Magnetic Resonance in Medicine

Open birdcage coil for head imaging at 7T

Anton V. Nikulin[1] ![ORCID] | **Alexandre Vignaud**[2] ![ORCID] | **Nikolai I. Avdievich**[3] ![ORCID] |
Djamel Berrahou[4] | **Julien de Rosny**[1] | **Abdelwaheb Ourir**[1]

[1]Institut Langevin, ESPCI Paris, CNRS, PSL University, Paris, France

[2]Université Paris-Saclay, CEA, CNRS, BAOBAB, NeuroSpin, Gif-sur-Yvette, France

[3]High-Field MR Center, Max Planck Institute for Biological Cybernetics, Tübingen, Germany

[4]Multiwave Innovation SAS, Marseille, France

Correspondence
Anton V. Nikulin, Institut Langevin, ESPCI Paris, CNRS, PSL University, Paris 75005, France.
Email: a.v.nikulin@live.ru

Purpose: To theoretically describe, design, and test the new geometry of the birdcage coil for 7 Tesla anatomical brain imaging, which includes a large window on top, without deliberately jeopardizing its homogeneity and efficiency. This *opencage* will not only improve patient comfort but also enable the volunteer to follow functional MRI stimuli. This design could also facilitate the tracking of patient compliance and enable better correction of the movement.

Methods: Via the transfer matrix approach, a birdcage-like coil with a nonperiodic distribution of rungs is constructed with optimized currents in the coil rungs. Subsequently, the coil is adjusted in full-wave simulations. Then, the coil is assembled, fine-tuned, and matched on the bench. Finally, these results are confirmed experimentally on a phantom and in vivo.

Results: Indeed, the computed isolation of −14.9 dB between the feeding ports of the coil and the symmetry of the circular polarized mode pattern transmit RF magnetic field (B_1^+) showed that the coil was properly optimized. An experimental assessment of the developed coil showed competitive transmit efficiency and coverage compared with the conventional birdcage coil of similar size.

Conclusion: The proposed opencage coil can be designed and work without a dramatic drop of performance in terms of the B_1^+ field homogeneity, transmit efficiency ($\langle B_1^+ \rangle / \sqrt{P_{ref}}$), peak local specific absorption rate (SAR_{10g}) and SAR efficiency ($\langle B_1^+ \rangle / \sqrt{SAR_{10g}}$).

KEYWORDS
birdcage coil, brain imaging, head coil, open coil, ultra-high field MRI

1 | INTRODUCTION

One of the most common volume RF coils in MRI is the birdcage coil, which is typically used as a transmit coil.[1,2] Large body birdcage coils are inserted into the bore of MRI up to 3 T. Human head birdcages are also used to image patients with stereotaxic frames in a presurgery phase or postsurgery after the installation of active implants (eg, deep brain stimulator).[3] At 7T, although they have demonstrated limitations in providing homogeneous excitation,[4] head birdcages are

largely used for most neurological applications both for ^{1}H imaging and for x-nuclei imaging.[5] Whereas birdcages are efficient transmit coils, they are usually shielded. Therefore, they hinder access to the patients, reducing their comfort and making the MRI examination more stressful, especially if the patient suffers from claustrophobia. Better accessibility for the patient or volunteer would also help during cognitive functional MRI experiments, especially to see the visual stimuli shown on a screen on the back of the magnet bore.[6] Moreover, a larger window in front of the patient face would make a motion tracking device more reliable.[7] Finally, this spacing would be useful for MRI-guided surgery (eg, laser interstitial thermal therapy), which uses a laser device for selective ablation of a lesion or a tissue.[8]

To provide a larger opening in front of patients' faces, various half-volume RF coils are available, such as half-birdcage coils,[9] U-shaped birdcage coils,[10] and quadrature half-volume transverse electromagnetic coils.[11] However, the transmit RF magnetic field (B_1^+) coverage for the aforementioned coils is only half that of a conventional birdcage coil.

An alternative to resolve the stated issue is to use phased array coils in the transmit regime. Indeed, the geometry of phased arrays can be shaped almost at will if its elements are well decoupled.[12-14] Despite all the advantages of phased arrays, the conventional birdcage coil still remains the most used and most reliable for the transmit regime, even at Ultra-High Field MRI such as 7T, because of the complexity and costliness of the arrays. In contrast, in the receive regime, the usage of phased arrays is preferable because of the SNR gain provided by the arrays.[15] In this work, as a proof of concept and for simplicity we use the developed open birdcage coil as a transceiver.

Another option for creating a large window would be to remove the shield and decrease the number of birdcage rungs (legs), but that option leads to loss of homogeneity[16] of the B_1^+ field and an increase in the specific absorption rate (SAR), as shown below. Hence, designing an efficient RF coil that is able to provide this window on the head without these flaws is a utility task to be resolved. For that purpose, a birdcage coil was proposed with few rungs at the top side to open a window in front of the face of the patient. We named this RF coil an *opencage*. The proposed coil necessitates the realization of an aperiodic structure with a given current distribution on the rungs. Previously, as a test of this idea we built a small prototype working at 300 MHz. This preclinical coil was successfully tested to image a rodent head at 7T.[17] In the current contribution, we propose a much larger prototype dedicated to Ultra-High Field human brain imaging at 7T. In contrast to the first prototype working in linear polarization mode, this prototype is driven in circularly polarized (CP) mode. To feed the birdcage coil in CP mode, the 2 linear orthogonal modes need to be driven. Because the birdcage is symmetrical, the isolation coefficient between the 2 feeding ports exciting the

linear modes is low. However, this rule is not valid by default for the developed opencage coil because the coil is not symmetrical along its horizontal plane. Therefore, theoretical and numerical optimization and utilization of the prototype should be performed with high accuracy and tolerance.

This paper starts with the methods section, where the electrical model of the coil is introduced. From this model, the values of the equivalent capacitors and inductances are derived and checked with a lumped element circuit simulator. Based on these values, the geometry of the opencage coil is deduced and adjusted in a full wave simulator. The prototype assembly is then described, and the method to test this is explained. The results section begins with the results obtained from the full-wave simulation. Then, it presents experimental results obtained with a spherical phantom and the head of a healthy volunteer. Finally, the results are discussed.

2 | METHODS

2.1 | Equivalent model of the coil and calculations of the currents

One solution to set the current distribution was used early to develop elliptical,[18,19] or oval birdcage coils.[20] However, this approach is not suitable for an arbitrary distribution of the rungs. To that end, we propose an approach wherein the opencage coil is considered as a transmission line-based coil in which we adjust the phase shift per unit cell and the characteristic impedance between different parts of the transmission line. Indeed, similar to a birdcage coil, an opencage coil is made of N unit cells. A unit cell is composed of an arrangement of parallel rungs that are interconnected by end-rings. The B_1 field results mainly from the current that flows across the rungs. Here, because we need to generate the CP mode as in the conventional birdcage coil, we use the same rule to choose the complex current values; that is, the current phase is set to be equal to the angular position of the rungs for the $k = 1$ mode. In contrast to the birdcage coil, the rungs in the opencage coil are not equidistant, and the electrical design of the new coil cannot be based on conventional methods. Indeed, our aim here is to design a coil composed of 8 rungs at the bottom that are separated by 22.5°, and only 2 rungs at the top separated by 90°, wherein an opening is provided as shown in Figure 1A. The equivalent and general electrical model is shown in Figure 1B. According to Ref. 21, a unit cell (a red rectangle in Figure 1B,C) can be described by a 2×2 transmission matrix or an ABCD matrix. Its expression is given by

$$T_i = \begin{pmatrix} 1 + Z_i Y_i & -\dfrac{Z_i^2 Y_i + 2Z_i}{2} \\ -2Y_i & 1 + Z_i Y_i \end{pmatrix}, \tag{1}$$
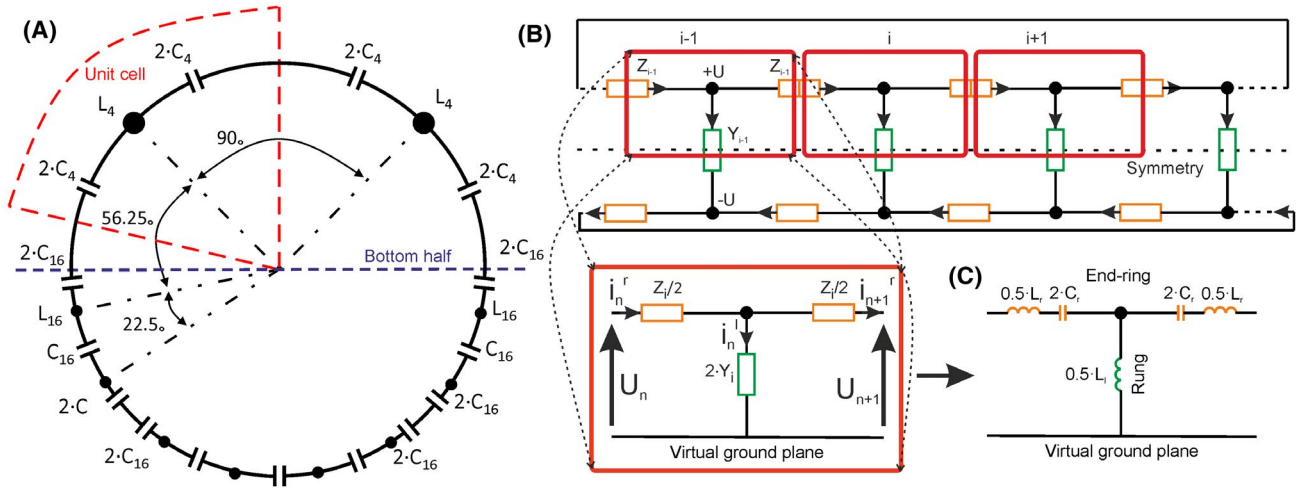
FIGURE 1   (A) Simplified (transverse) sketch of an opencage composed of 10 rungs. Here, 8 rungs are at the bottom and 2 rungs are at the top. (B) Equivalent electrical circuit of an opencage. A rung and end-ring segment (both together is the unit cell) are represented inside the red rectangles. A detailed unit cell is shown in the insert (B). (C) High-pass unit cell corresponding to the actual unit cell of the opencage coil

where Z_i and Y_i are the impedance and admittance of the i-th unit cell, respectively. Because the unit cell border intersects the rung and the end ring into 2 equal halves (Figure 1B), only half of the impedance or half of the inductance is considered. From the eigenvalue and eigenvector analysis[16,21] of T_i, 2 fundamental properties of the unit cell can be computed: the Bloch impedance (Z_i^b) and the relative phase shift ($\delta\varphi_i$). Their expressions are given by

$$\delta\varphi_i = \cos^{-1}\left(1 + Z_i Y_i\right) \qquad (2)$$

and

$$Z_i^b = \frac{1}{2}\sqrt{Z_i^2 + \frac{2Z_i}{Y_i}}. \qquad (3)$$

Hence, the aim is to set Z_i and Y_i to obtain a phase shift that corresponds to the geometrical angle. However, the phases should also be chosen to generate the CP mode (other modes are shown in section 1 of the Supporting Information). To that end, no reflection should occur between the unit cells; that is, the Bloch impedance must be the same along all unit cells.

To move forward, the expressions of Z_i and Y_i are required. They are given by the electrical model of the unit cell shown in Figure 1C. The values L_i^l and L_i^r are the equivalent inductances of the rung and end rings, respectively. To overcome this inductive effect, 2 lumped capacitors of value C_i are inserted into the end rings.

From this modelling and Equations (2) and (3), the rung inductance and ring capacitance can be deduced directly as:

$$L_i^l = \frac{4\left(Z_i^b\right)^2 \left(1 - \cos\delta\varphi_i\right) - 2L_i^r Z_i^b \left|\sin\delta\varphi_i\right|\omega}{2Z_b \left|\sin\delta\varphi_i\right| \left(1 - \cos\delta\varphi_i\right)\omega - L_i^r \sin^2\delta\varphi_i\omega^2}$$

$$C_i = \frac{L_i^r \left(\cos\delta\varphi_i + 1\right)\omega - 2Z_i^b \left|\sin\delta\varphi_i\right|}{\left(L_i^r\right)^2 \left(\cos\delta\varphi_i + 1\right)\omega^3 + \left(Z_i^b\right)^2 \left(4\cos\delta\varphi_i - 4\right)\omega},$$

where Z_i^b is the Bloch impedance of the opencage. To compute the equivalent inductance, one needs to define the coil geometry. Our aim is to design an opencage coil for Ultra-High Field head anatomical imaging at 7T operating at a frequency of 298 MHz. Hence, we set the geometrical parameters to an inner radius of 130 mm, a length of 240 mm, and a shield radius of 155 mm. The rungs and end rings consist of metallic rectangular tracks. Sketches of the coil are shown in Figure 1A.

The mutual and self-inductances were estimated in accordance with Ref. 22 and Ref. 23. In particular, the mutual inductances of the rungs were estimated using the rule for 2 parallel wires.[22] With the image theorem, the effect of the shield was also taken into account.[22] The inductance of the rings was estimated according to the rule for 2 tilted wires.[22]

In the following, to highlight the importance of impedance matching between the unit cells, we test 3 different unit cells. The first unit cell is tuned to have a phase shift of 22.5° (as for 16-rung birdcage). The widths of the rung and ring are both equal to 10 mm. The phase shift of the second and third unit cells equals 90° (as for 4-rung birdcage). For the second unit cell, the widths of the rung and ring are also equal to 10 mm. Thus, the Bloch impedance does not match that of the 22.5° phase shift unit cell. In contrast, for the third unit cell the width of the rung is modified to be the same. The capacitance, inductances, Bloch impedance, and rung width values are shown in Table 1.

Element	22.5° Cells (as for 16 rungs)	90° Cells (as for 4 rungs)	Modified 90° Cells
C_r(pF)	5.15	0.95	1.23
L_t(nH)	173.97	132.6	66.7
L_r(nH)	42.09	165.4	165.4
Rung width (mm)	10	10	39.5
Bloch impedance (Ω)	62.45	124.1	62.45

TABLE 1 Values of the capacitances (C_r), effective rung inductances (L_l), and effective ring inductances (L_r)
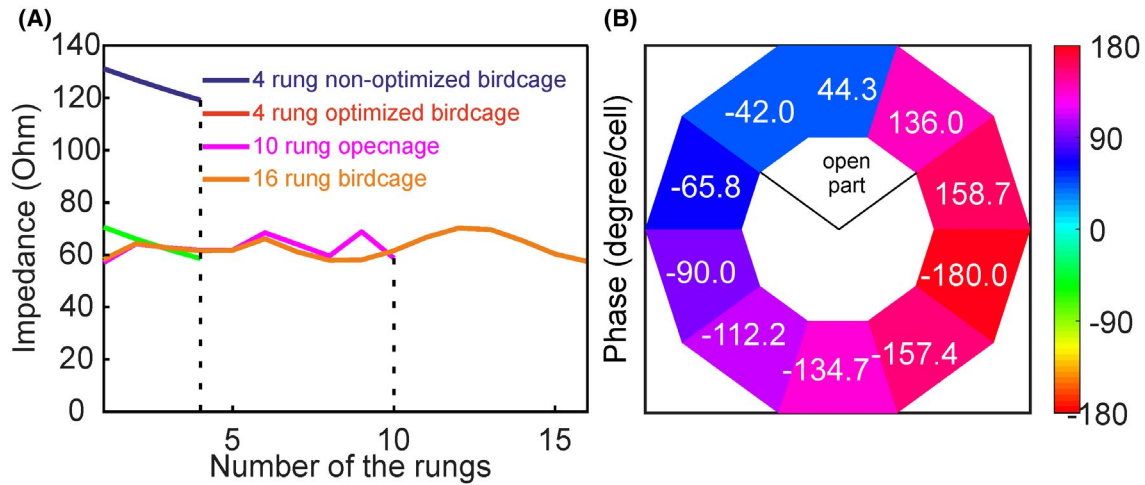
FIGURE 2 (A) Impedance in end-ring nodes for several birdcages composed of different unit cells. (B) Current distribution in end-ring segment

2.2 | Circuit simulations

Additional electrical simulations using the circuit simulator of the CST Microwave Suite 2019 (Dassault Systèmes, Vélizy-Villacoublay, France) were performed to validate these estimated theoretical values of the impedance and phases. Here, 3 different birdcages and 1 opencage were studied: a 16-rung birdcage (22.5° unit cells), a 4-rung birdcage (90° unit cells) without Bloch impedance matching, a 4-rung birdcage (modified 90° unit cells) with Bloch impedance matching, and an opencage (combination 22.5° unit cells and modified 90° unit cells). Here, the opencage was modelled as a 10-unit cell circuit. First, the Bloch impedance was assessed by plotting the ratio between the voltage and current at the nodes of the unit cells (Figure 2A). As expected, when the 90° phase shift cell was matched, the Bloch impedance was the same as that of 22.5° cell. Second, Figure 2B shows that the phases along the unit cells of the opencage coil were consistent with the expected phases. As a result, the coil can now be designed more precisely and investigated in full-wave simulations.

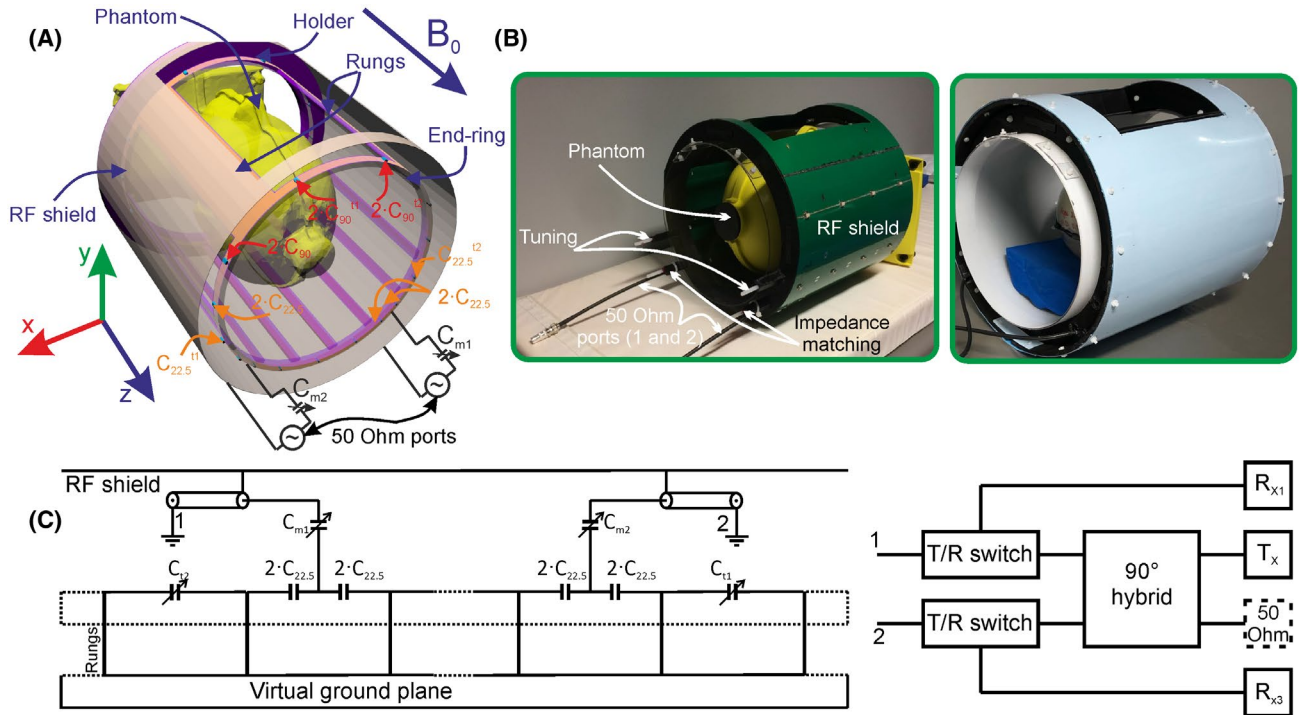## 2.3 | Design of the opencage coil

The opencage design is illustrated in Figure 3A. Here, we introduce $C_{22.5°}$ and $C_{90°}$, the values of the capacitors of the

22.5° and 90° unit cells. To generate the CP mode, the coil is driven in quadrature by 2 50 Ohm ports that are 90° apart at the bottom (Figure 3A). The ports are connected between the doubled capacitances in the end-ring segments and the shield, as shown in Figure 3A. Additionally, 2 trim capacitors—C_{t1}, C_{t2} and C_{m1}, C_{m2}—are inserted for frequency tuning and input impedance matching of the coil.

The geometrical parameters of the coil were specified in the previous section to fit an average human head. However, to provide access, a gap of 139 mm is created in the copper shield between the 2 separated 90° rungs.

2.4 | Full-wave numerical simulations

The design was numerically tested and optimized using commercial electromagnetic software CST Studio Suite 2019 (Dassault Systèmes, Vélizy-Villacoublay, France). The coils was modeled using 35-μm copper strips. In the conducted simulations, the coil was first loaded with a homogeneous dielectric spherical phantom with a diameter of 165 mm (not shown in Figure 3A). Its relative permittivity (ε_r) and conductivity (σ) were equal to 75 and 1 S/m, respectively. The simulations also included the RF shield, placed on the lossy FR4 substrate (Figure 3A) from the CST library, and the coil holder made of lossless polylactic acid (PLA) with

FIGURE 3 (A) Geometry of the loaded opencage coil driven in quadrature. (B) Photograph of the opencage coil (uncovered: left, covered: right). (C) Sketch of the tuning, matching, and interfacing circuits
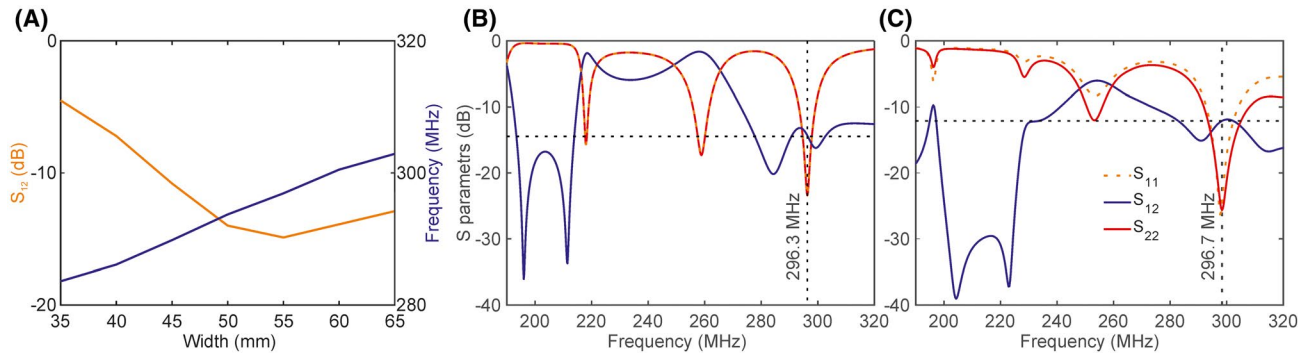

FIGURE 4 (A) Simulated isolation (left axis) and resonant frequency (right axis) as a function of the top rung width. (B) S-parameters of the opencage obtained in the full-wave simulations. (C) measured S-parameters

permittivity of 3.5. These simulations were performed using the finite element method-based frequency domain solver with approximately 1 million mesh cells.

With the capacitance and inductance deduced from the analytical model, the resonance frequency of the simulated unloaded opencage coil was 288.6 MHz instead of 298 MHz. However, the isolation between the ports was only −6.3 dB. Nevertheless, after adding equivalent series Inductance and equivalent series resistance of the of the used capacitors, phantom, gap in the shield, substrate, and the holder, the resonant frequency shifts to 278.3 MHz. The contribution of each addition is shown in the supplementary materials (Section 2). Thus, to tune the coil to a frequency of 298 MHz, the capacitors values must be decreased compared to the analytical values. As a result, $C_{90°}$ becomes 1

pF instead of 1.23 pF; $C_{22.5°}$ becomes 4.2 pF instead of 5.15 pF. Finally, to maximize the isolation between the 2 feeding ports, we conducted an additional simulation sweep of the top rung width using the FEM-based frequency domain solver (Figure 4A). In this simulation, the coil was loaded by the spherical phantom. The holder and substrate were also included. The width of the top rungs was varied from 35 mm to 65 mm. Based on to this parameter sweep, the final width becomes 55 mm instead of 39.5 mm. Moreover, to reduce the number of capacitors, some pairs of capacitors in series were replaced by a single capacitor. According to Figure 3, twofold capacitances were retained only on the end rings, wherein the feeding ports were connected, the 2 types of cells were connected, and the cells were on top part (capacitance segmentation).
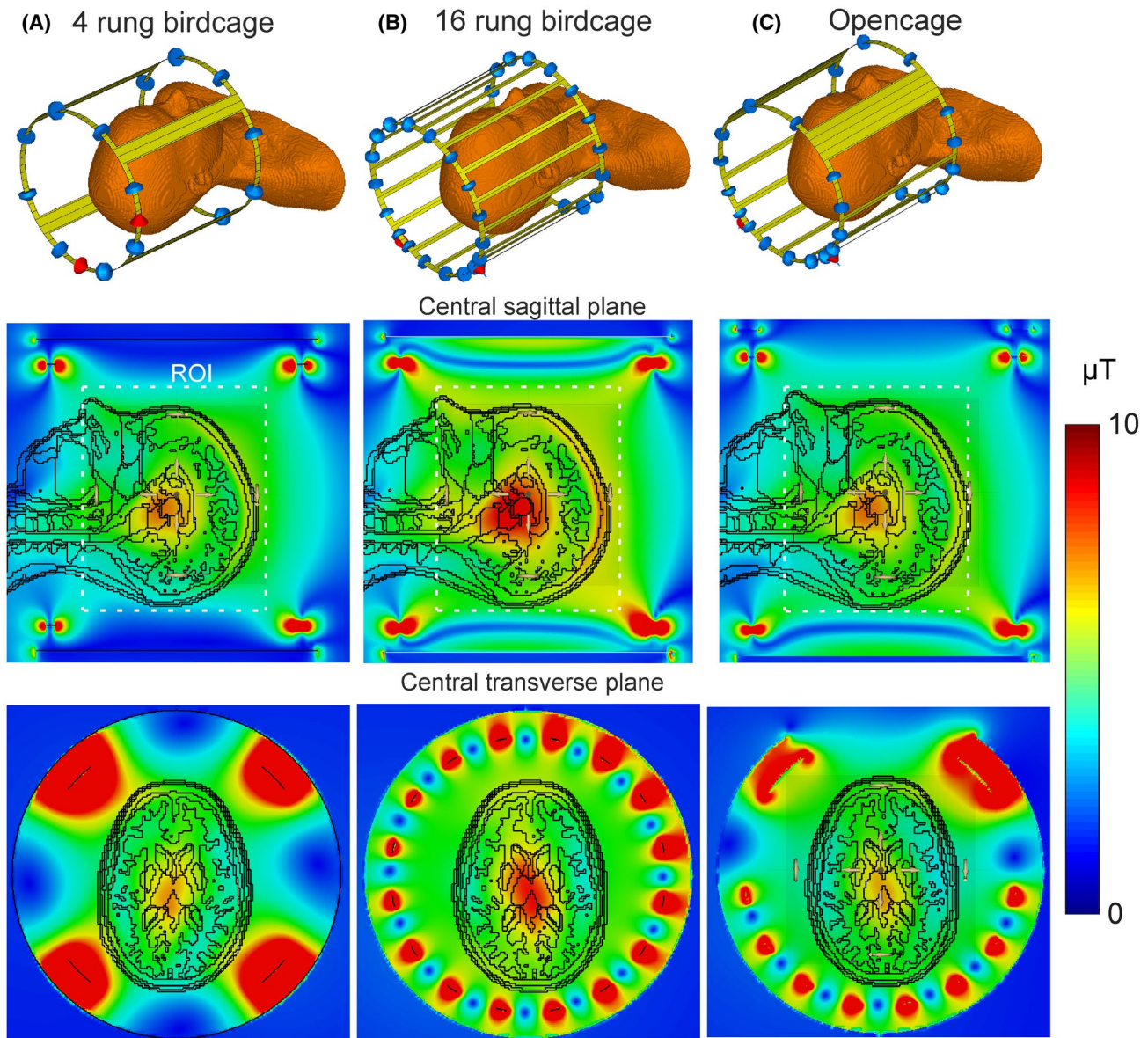
FIGURE 5 (A) B_1^+ maps obtained via numerical computation for the 4-rung birdcage coil. (B) Simulated B_1^+ maps for the birdcage coil of 16 rungs. (C) Simulated B_1^+ maps for the opencage coil. The RF shield is hidden in all the setups. The top row shows the simulated setup. The maps obtained in the central sagittal plane are depicted in the middle. The bottom line shows the fields in the central transverse plane. For comparison purposes, all maps were normalized to the reference power of the opencage coil obtained experimentally and mentioned below. The ROI used for the field statistical evaluation is indicated by the white dashed rectangle in the sagittal slice. The full size of the ROI is 150 mm along the X axis, 205 mm along the Y axis, and 180 mm along the Z axis. ROI, region of interest

We compared the transmit efficiency ($B_1^+/\sqrt{P}$), B_1^+ homogeneity using a normalized SD, peak B_1^+ deviation (p B_1^+), local maximal peak SAR averaged over 10 grams of tissues, and SAR efficiency ($\langle B_1^+ \rangle/\sqrt{SAR_{10g}}$) of the opencage to those of the 2 birdcage coils comprising 4 and 16 rungs. The simulated coils had the same size, except for the width of the rungs, which was different in these coils, namely, 20 mm for the birdcage with 4 rungs and 10 mm for the birdcage with 16 rungs. In these simulations, we used the time domain solver of CST Microwave Suite 2019 (Dassault Systèmes) with approximately 8 to 10 million of mesh cells.

Instead of a spherical phantom, we used the multi-tissue Ella voxel model.[24-26] This model, cropped at the shoulder level, had an isotropic voxel of 2 mm³. In all simulation series, the coils were tuned and matched using an electrical simulator extension (CST Schematic by Dassault Systèmes). Finally, we evaluated the radiated power for each coil to study the effect of the opening. For this comparison, we evaluated the coil for 1 W of stimulated power. However, to compare the simulated (Figure 5) and measured maps, the first maps were normalized to the same reference power as that of the experiment.

2.5 | Prototype assembly

Photographs of the coil are presented in Figure 3B. The frame of the coil was 3D-printed using polylactic acid. The electrical tracks were made of 35 μm-thick copper tape AT526 (Advance Tapes International Ltd, Leicester, England). The RF shield was chemically etched on the FR4 substrate with 5 narrow gaps made along the Z axis in the metal layer to prevent eddy currents. For that purpose, 4 nonmagnetic capacitors of 1 nF were soldered between these gaps as proposed in Ref. 27.

In the prototype, we used the same values of the capacitors as those of the simulation. For the assembly, we used 1500 V "B-"size capacitors of SH series (Exxelia, Paris, France). The tuning and matching circuits were implemented as shown in Figure 3A,C. Two trim capacitors AT 57250 of 1-13 pF (Exxelia, Paris, France) connected in series to the feeding lines were employed for impedance matching. To tune the resonant frequency, the same variable capacitors were also placed instead of 2 fixed capacitors as shown in Figure 3C.

To connect the coil to our 7T MRI scanner (Siemens Healthineers, Erlangen, Germany), interfacing device with the principal sketch shown in Figure 3C was used. In this interface, 2 ports of the coil were connected to a 90°hybrid coupler to achieve circular polarization in the transmit regime. In the receive regime, each port of the coil was connected to its own receive channel.

2.6 | Experimental evaluation

First, the assembled opencage coil was assessed on a bench equipped with a vector network analyzer (Anritsu MS46122b, Anritsu, Atsugi, Japan) via S-parameters measurements. The coil loaded by the spherical phantom of 165-mm diameter (agar 3%m, NaCl 0.5%m, NiCl$_2$ 0.03%m) was tuned and matched slightly below the exact Larmor frequency of 297.3 MHz, namely, at 296.7 MHz. Because of the opening in the RF shield, we observed a frequency shift of about +0.5 MHz after placing the coil inside the MRI scanner bore. This shift occurs due to an interaction with an RF shield embedded to the MRI scanner. Therefore, we anticipate the ability of the MRI bore to slightly shift the coil frequency. Then, the coil loaded by the spherical phantom was installed and connected to our MRI scanner using the interface described above. A magnetization prepared turbo-FLASH–based sequence, also called XFL, was employed for flip angle mapping,[28] which was later converted to the B_1^+ maps. Along a sagittal orientation, 22 slices spaced 4 mm apart were acquired with the following parameters: TR/TE = 20000/3.06 ms, 4 mm isotropic voxels, global FOV 256 × 256 × 168 mm^3, excitation flip angle of 7°, and saturation flip angle of 60°. The same sequence was also used with a commercial birdcage coil of 16 rungs (Invivo Corporation, Gainesville, FL).[29] The commercial birdcage coil used has a 3.3% smaller inner volume (radius of 140 mm and length of 200 mm) compared to our prototype (radius of 130 mm and length of 240 mm). For both coils, we adjusted the input peak power via the same B_1^+ mapping sequence, allowing us to obtain a 500 μs rectangular 90° pulse in the center of the phantom. This input peak power (P_{ref}) was calibrated to the input of the coil, taking into account a loss of 0.845 dB in the coil interface and 1.9 dB in the cables. Based on the whole phantom maps, we evaluated transmit efficiency ($B_1/\sqrt{P_{ref}}$) and homogeneity of the B_1^+ field via the SD divided by the mean B_1^+, that is, SD/$\langle B_1^+ \rangle$ for both coils.

Finally, in vivo images and B_1^+ maps of a healthy volunteer's head were acquired for the birdcage and for the opencage coil using the *restricted SAR protocol* utilized onsite to test new coil prototypes. The experiments were performed under both our institutional review board and national ethical committee approvals. The rationale and sequence protocol are presented in Ref. 30. Written consent of the volunteer was obtained beforehand at the beginning of the MR acquisitions. Afterward, the obtained images were filtered using the amplitude of the flip angle map and smoothed with a median filter. The B_1^+ maps were also smoothed with a median filter. For these obtained data, we also estimated the transmit efficiency ($\langle B_1^+ \rangle/\sqrt{P_{ref}}$) and homogeneity via SD/$\langle B_1^+ \rangle$. To assess the overall transmit efficiency and homogeneity, we used the average value over the 3 orthogonal slices.

3 | RESULTS

3.1 | Numerical optimization of the coil

First, we applied the parameters obtained analytically, and then we optimized the width of the top rung in the opencage coil loaded with the spherical phantom. To that end, we plotted the (S_{12}) isolation between the feeding ports depending on the width (Figure 4A). The lowest S_{12} coefficient of −14.9 dB appears for a width of approximately 55 mm instead of the initial width of 39.5 mm. Moreover, this increase in the rung width (ie, decrease in inductance) was used to shift the resonant mode toward the desired Larmor frequency of 297.2 MHz without additional reduction the capacitance. Figure 4B depicts the final S-parameters of the simulated coil.

The B_1^+ maps of the opencage (Figure 5C) was compared to the birdcage coils containing 4 (Figure 5A) and 16 rungs (Figure 5B). A quantitative assessment of the efficiency of each simulated coil is arranged in Table 2. The conducted simulations (Figure 5) showed that the developed opencage coil and 16-rung birdcage coils provided 7% better homogeneity of B_1 assessed via SD/$\langle B_1^+ \rangle$ compared to 4-rung birdcage (Table 2). Field homogeneity assessed with peak

TABLE 2 Numerical comparison of different volume coils for 1W of stimulated input power

Coil	$\langle B_1^+ \rangle / \sqrt{P}$ (μT/$\sqrt{W}$)	(W/kg)	SD/$\langle B_1^+ \rangle$	pB_1^+	$\langle B_1^+ \rangle / \sqrt{SAR_{10g}}$	P_r (W)
4 rung birdcage	0.358	0.599	0.263	0.522	0.463	0.176
16 rung birdcage	0.370	0.458	0.245	0.518	0.547	0.166
Opencage	0.365	0.519	0.245	0.507	0.507	0.216
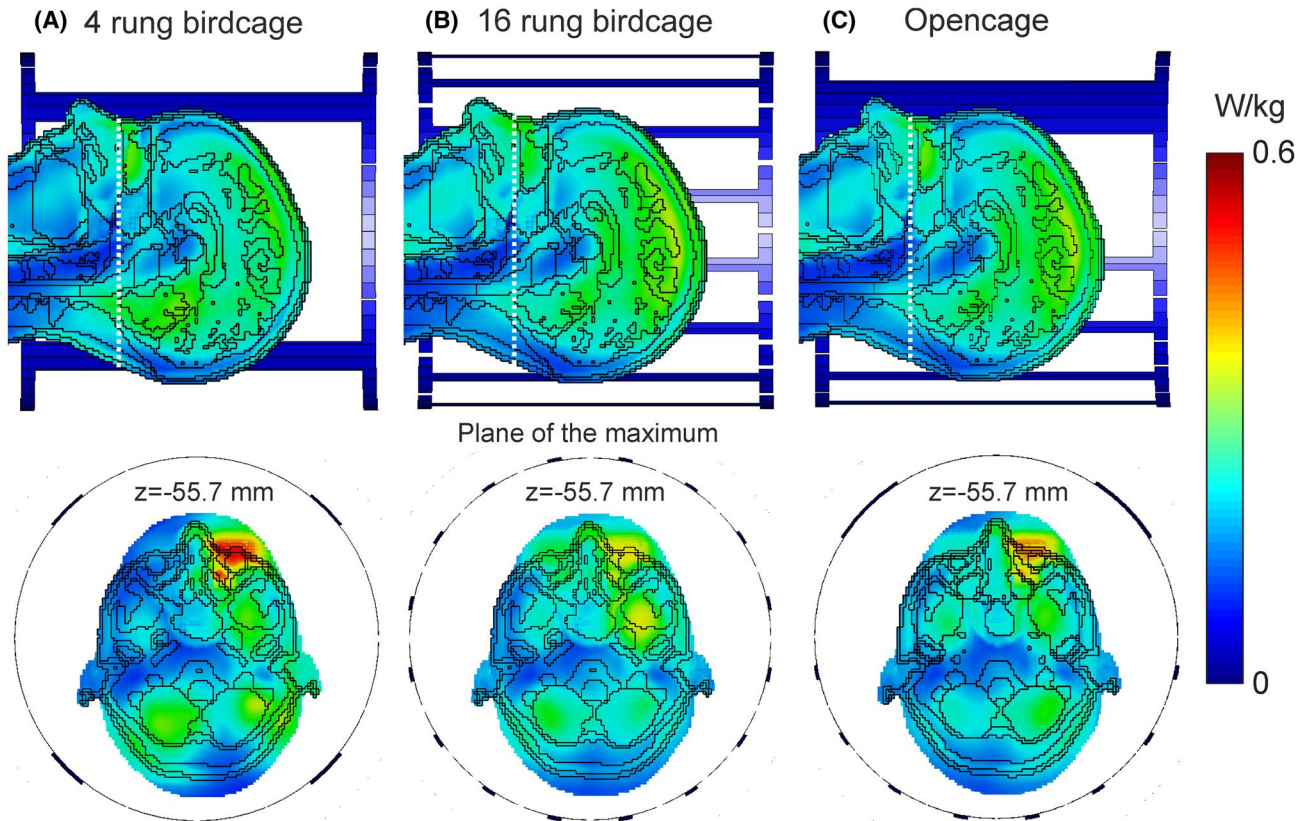
FIGURE 6 (A) Numerically estimated local SAR for 10 g of tissues for the 4-rung birdcage coil, (B) for the 16-rung birdcage coil, and (C) for the opencage coil. All maps were normalized for 1 W of stimulated power. Top row shows the maps in the central sagittal plane. Bottom row presents the maps of the transverse plane of the maximum. The position of the maximum is shown by the white dashed line, with a z coordinate of −55.7 mm. SAR, specific absorption rate

B_1^+ deviation was comparable (within 3%) for all 3 coils, as shown in Table 2. The average transmit efficiency was very similar to all 3 coil configurations (within 3%).

The quantitative analysis of the SAR is summarized in Table 2 and plotted in Figure 6. One observes the 2 SAR spots, with the lowest spot in the head vertex. In this area, the SAR insignificantly increases as the number of rungs decreases, as can be observed in the top row of Figure 6. However, we should pay attention to the strongest spot, which is observed close to the nose. The values observed in this region correspond to the maximal seen in the phantom. Therefore, the values for this region are shown in Table 2. In this case, the SAR efficiency increases with an increase of the number of the birdcage rungs. For example, the 16-rung birdcage shows the best SAR efficiency. Also, the 10-rung opencage

demonstrates 7.3% worse SAR efficiency compared to the 16-rung birdcage, and 8.7% higher SAR efficiency compared to the 4-rung birdcage. Therefore, one can conclude that the opencage provides a compromise in terms of the SAR efficiency between the 4-rung and 16-rung birdcages.

3.2 | Imaging with the opencage coil

First, the coil was tuned to a frequency of 297.2 MHz and matched in the presence of the spherical agar phantom at a level of −26 dB, with the isolation level between the ports being −12.5 dB (Figure 4C). Subsequently, we measured the B_1^+ field inside the spherical phantom using the opencage and commercial birdcage coil (see Figure 7B,C). For comparison

B_1^+ field magnitude (µT)
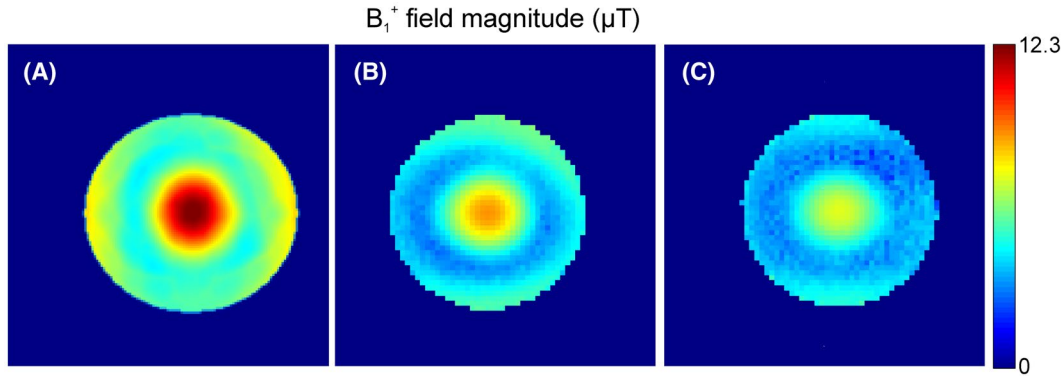
FIGURE 7 (A) Central sagittal slice of the B_1^+ field of the spherical phantom obtained by simulation of the opencage coil, (B) measured using the opencage coil, (C) and measured using the commercial birdcage coil
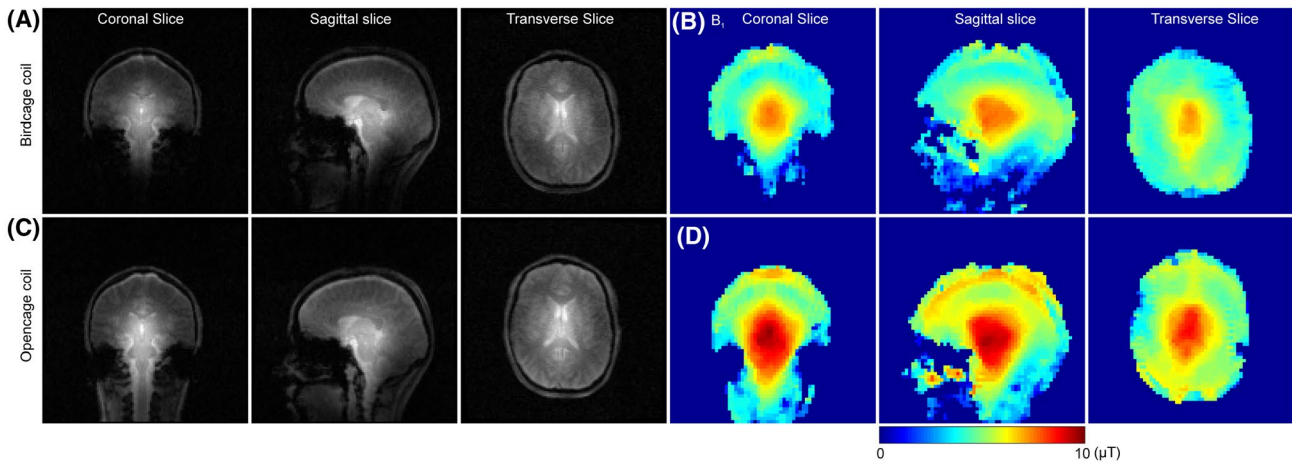
FIGURE 8 (A) In vivo images (a.u.) of the brain obtained in the 3 central slices for the birdcage coil. (B) B_1^+ maps (µT) obtained with the birdcage coil in 3 slices. (C) In vivo images from 3 slices for the opencage coil. (D) B_1^+ maps obtained with the opencage coil

purposes, the map of B_1^+ obtained by simulation of the opencage coil is also shown in Figure 7A. From the experimental maps, we estimated that the mean transmit efficiency ($\langle B_1^+ \rangle$ /$\sqrt{P_{ref}}$) of the birdcage equals 0.133 µT/$\sqrt{W}$, corresponding to $\langle B_1 \rangle$ of 3.98 µT; and 0.189 µT/$\sqrt{W}$, corresponding to $\langle B_1^+ \rangle$ of 4.66 µT (6.07 µT obtained in the simulations) for the opencage. Here, the input peak power was 899 W for the commercial birdcage coil and 605.5 W for the opencage coil. According to the acquired data, we calculated SD/$\langle B_1^+ \rangle$ for both coils. The birdcage coil demonstrated a slightly better homogeneity of B_1^+ in the entire phantom. Indeed, SD/$\langle B_1^+ \rangle$ equals 0.214 for the birdcage coil and 0.223 for the opencage coil.

Finally, in vivo images and B_1^+ were acquired for the birdcage coil (Figure 8A,B) and for the opencage coil (Figure 8C,D). The mean transmit efficiency of the birdcage equals 0.13 µT/$\sqrt{W}$, corresponding to $\langle B_1 \rangle$ of 4.69 µT; and 0.194 µT/$\sqrt{W}$, corresponding to $\langle B_1 \rangle$ of 5.57 µT (5.38 µT obtained in the simulations) for the opencage coil. Here, the measured images were acquired with 1300.5 W as the reference peak

input power for the birdcage coil and 824.2 W as that for the opencage coil. In terms of homogeneity, the birdcage coil demonstrated slightly better results in the entire phantom. SD/$\langle B_1^+ \rangle$ equals 0.284 for the birdcage coil and 0.306 for the opencage coil.

4 | DISCUSSION

First, the results of the full-wave simulations show the robustness of the optimization strategy because the field distribution of the opencage coil corresponds to the conventional fundamental CP mode of the birdcage coil, with the maximum of the field in the center and decaying toward the periphery. The SAR efficiency is an important and critical parameter of the transmit coils involved in in vivo applications. Consequently, assessing the SAR (Figure 6), we confirmed the importance of the conducted optimization and clearly observed the benefits compared to the birdcage coil of only 4 rungs. An opening in the coil cannot be provided

simply by decreasing the number of rungs because of the SAR, which in the case of our opencage coil is a trade-off between the birdcage of 4 rungs and the birdcage of 16 rungs. However, this outcome was expected because in the birdcage-like coil, the electrical field is confined around the rungs. In the birdcage with 16 rungs, the electrical field is more smoothly distributed between the rungs, whereas it is more concentrated around the 90° rungs for both the 4-rung birdcage and opencage coils. In addition, smaller capacitances in the birdcage of 4 rungs also increase the electric field.

By analyzing the experimental data obtained with the spherical phantom (Figure 7), one can conclude that the opencage shows 4% worse homogeneity for the whole spherical phantom, assessed via $SD/\langle B_1^+ \rangle$, than that of the birdcage coil, and a 7.2% homogeneity drop for the in vivo acquisition (Figure 8B,D). In contrast, the simulations show comparable homogeneity via the SD in the voxel head phantom (Table 2). However, these 2 considered configurations cannot be compared directly because the coils have different sizes, whereas the simulated coils have the same size. Therefore, a comparison of these SD values obtained in vivo is more relevant.

The opencage is more efficient in transmit efficiency even though it has a 3.3% larger inner spacing. This dramatic enhancement in mean transmit efficiency of 49.2% for the spherical phantom and 42.1% for the in vivo case can be explained by the fact that the commercial coil used was not properly tuned after upgrading to the new gradient system. However, before the upgrade, the peak input peak power was 687.5 W for the same birdcage coil loaded with the same spherical phantom. Therefore, the performance drop would be less dramatic compared to the opencage coil, which needs a peak input power of 605.5 W to satisfy the FA in the phantom center. In addition, a longer inner spacing of the developed coil allows imaging of the upper C-spine that is not visible with the commercial birdcage coil used (Figure 8A,C).

The proposed open birdcage coil was mainly developed as a transmit coil. To further improve the SNR, the open birdcage coil can be combined with a multi-channel tight fit receive array placed inside the transmit coil. In addition, the proposed design could be adapted for dual nuclei operation by implementing a second nested structure, such as a second opencage, or by creating a band-pass or band-stop unit cell adjusted for 2 frequencies.[31] The low-pass or hybrid birdcages can also be constructed using the developed approach.[31]

5 | CONCLUSION

In this work, we proposed a new type of RF quadrature coil, named an *opencage*, that facilitates access to the region under study. This opening may be useful not only for improving patient comfort but also for facilitating cognitive functional MRI

experiments,[6] in imaging patients with a stereotaxic frame,[3] for making motion tracking devices more reliable,[7] and for carrying out MRI-guided laser interstitial thermal therapy.[8] In our investigation, this coil was optimized for head imaging at 7T. However, as shown earlier, the proposed approach is scalable and therefore could be used for constructing coils for other preclinical and clinical applications. The proposed RF coil is based on Bloch impedance matching and phase adjustment. The main parameters of the opencage coil were determined analytically, tested numerically, and confirmed experimentally on the bench and in MRI. Both numerically and experimentally, the opencage coil clearly demonstrated comparable behavior to the commercial birdcage coil.

ORCID
Anton V. Nikulin https://orcid.org/0000-0001-5640-8281
Alexandre Vignaud https://orcid.org/0000-0001-9203-0247
Nikolai I. Avdievich https://orcid.org/0000-0001-7608-0869

REFERENCES
1. Hayes CE, Edelstein WA, Schenck JF, Mueller OM, Eash M. An efficient, highly homogeneous radiofrequency coil for whole-body NMR imaging at 1.5 T. *J Magn Reson (1969)*. 1985;63:622-628.
2. Hayes CE. The development of the birdcage resonator: a historical perspective. *NMR Biomed*. 2009;22:908-918.
3. Golestanirad L, Kazemivalipour E, Keil B, et al. Reconfigurable MRI coil technology can substantially reduce RF heating of deep brain stimulation implants: first in-vitro study of RF heating reduction in bilateral DBS leads at 1.5 T. *PLoS One*. 2019;14:1-17.
4. Webb AG. Dielectric materials in magnetic resonance. *Concepts Magn Reson Part A Bridg Educ Res*. 2011;38A:148-184.
5. Hu R, Kleimaier D, Malzacher M, Hoesl MAU, Paschke NK, Schad LR. X-Nuclei imaging: current state, technical challenges, and future directions. *J Magn Reson Imaging*. 2020;51:355-376.
6. Huang RS, Sereno MI. Visual stimulus presentation using fiber optics in the MRI scanner. *J Neurosci Methods*. 2008;169:76-83.
7. Frost R, Wighton P, Karahanoğlu FI, et al. Markerless high-frequency prospective motion correction for neuroanatomical MRI. *Magn Reson Med*. 2019;82:126-144

8. Salem U, Kumar VA, Madewell JE, et al. Neurosurgical applications of MRI guided laser interstitial thermal therapy (LITT). *Cancer Imaging*. 2019;19:65.

9. Ballon D, Graham MC, Miodownik S, Koutcher JA. A 64 MHz half-birdcage resonator for clinical imaging. *J Magn Reson (1969)*. 1990;90:131-140.

10. Hudson AMJ, Köckenberger W, Bowtell RW. Open access birdcage coils for microscopic imaging of plants at 11.7T. *MAGMA*. 2000;10:69-74.

11. Peshkovsky AS, Kennan RP, Fabry ME, Avdievich NI. Open half-volume quadrature transverse electromagnetic coil for high-field magnetic resonance imaging. *Magn Reson Med*. 2005;53:937-943.

12. Avdievich NI. Transceiver-phased arrays for human brain studies at 7 T. *Appl Magn Reson*. 2011;41:483-506.

13. Sengupta S, Roebroeck A, Kemper VG, et al. A specialized multi-transmit head coil for high resolution fMRI of the human visual cortex at 7T. *PLoS One*. 2016;11:e0165418.

14. Clément J, Gruetter R, Ipek Ö. A combined 32-channel receive-loops/8-channel transmit-dipoles coil array for whole-brain MR imaging at 7T. *Magn Reson Med*. 2019;82:1229-1241.

15. Wiggins GC, Wiggins CJ, Potthast A, et al. A 32 channel receive-only head coil and detunable transmit birdcage coil for 7 Tesla brain imaging. In Proceedings of the 14th Annual Meeting of ISMRM, Seattle, WA, 2006. p. 415.

16. Mispelter J, Lupu M, Briguet A. *NMR Probeheads for Biophysical and Biomedical Experiments: Theoretical Principles and Practical Guidelines*. 2nd ed. London, UK: Imperial College Press; 2015.

17. Nikulin A, De Rosny J, Haliot K, Larrat B, Ourir A. Opencage radio frequency coil for magnetic resonance imaging. *Appl Phys Lett*. 2019;114:053503.

18. Li S, Collins CM, Dardzinski BJ, Chin CL, Smith MB. A method to create an optimum current distribution and homogeneous B1 field for elliptical birdcage coils. *Magn Reson Med*. 1997;37:600-608.

19. Leifer MC. Theory of the quadrature elliptic birdcage coil. *Magn Reson Med*. 1997;38:726-732.

20. De Zanche N, Yahya A, Vermeulen FE, Allen PS. Analytical approach to noncircular section birdcage coil design: verification with a Cassinian oval coil. *Magn Reson Med*. 2005;53:201-211.

21. Caloz C, Itoh T. *Electromagnetic Metamaterials: Transmission Line Theory and Microwave Applications. The Engineering Approach*. Hoboken, NJ: John Wiley & Sons; 2006.

22. Grover FW. *Inductance Calculations: Working Formulas and Tables*. Mineola, NY: Dover Publications; 2013.

23. Pascone R, Vullo T, Farrelly J, Cahill PT. Explicit treatment of mutual inductance in eight-column birdcage resonators. *Magn Reson Imaging*. 1992;10:401-410.

24. Li X, Rispoli JV. Toward 7T breast MRI clinical study: safety assessment using simulation of heterogeneous breast models in RF exposure. *Magn Reson Med*. 2019;81:1307-1321.

25. Rispoli JV, Wright SM, Malloy CR, McDougall MP. Automated modification and fusion of voxel models to construct body phantoms with heterogeneous breast tissue: application to MRI simulations. *J Biomed Graph Comput*. 2017;7:1.

26. IT'IS Foundation. *Overview: Database of Tissue Properties*. Available at: https://itis.swiss/virtual-population/tissue-properties/overview/. Accessed March 1, 2021.

27. Alecci M, Jezzard P. Characterization and reduction of gradient-induced eddy currents in the RF shield of a TEM resonator. *Magn Reson Med*. 2002;48:404-407.

28. Chung S, Kim D, Breton E, Axel L. Rapid B1+ mapping using a preconditioning RF pulse with turboFLASH readout. *Magn Reson Med*. 2010;64:439-446.

29. Saylor CA, inventor; Invivo Corp, assignee. *High-Field Mode-Stable Resonator for Magnetic Resonance Imaging*. US patent US7345482B2. March 18, 2008.

30. Vignaud A, Mauconduit F, Gras V, et al. Fast and unconditionally safe in vivo MR head protocol for home-made coil prototype assessment at 7T. *J Phys: Conf Ser*. 2018;1092:012159.

31. Nikulin A. *Volume RF Coils Based on Metamaterials for Ultra-high Field Magnetic Resonance Imaging* [Dissertation]. Paris: Institut Langevin, ESPCI Paris, CNRS, PSL University; 2020.

SUPPORTING INFORMATION

Additional Supporting Information may be found online in the Supporting Information section.

FIGURE S1 A, S-parameters, and H-field patters for the modes of the 16-rungs high-pass birdcage coil. B, S-parameters, and H-field patters for the modes of the 16-rungs high-pass opencage coil. For these simulations, the opencage coil was simplified as much as possible, that is, ie, ESR, ESL, phantom, holder and substrates were excluded. Thereby, spectrum slightly differs compared to Figure 4 of the manuscript. These simulations were done using Frequency Domain Solver

TABLE S1 Resonant frequency and S_{12} depending on the condition of the simulation